Chapter 7

Determining the Complex Refractive Index of Materials in the Far-Infrared from Terahertz Time-Domain Data

Maxime Bernier, Frédéric Garet and
Jean-Louis Coutaz

Additional information is available at the end of the chapter

http://dx.doi.org/10.5772/66348

Abstract

Terahertz time-domain spectroscopy is a well-established technique to study the far-infrared electromagnetic response of materials. Measurements are broadband, fast, and performed at room temperature. Moreover, compact systems are nowadays commercially available, which can be operated by nonspecialist staff. Thanks to the determination of the amplitude and phase of the recorded signals, both refractive index and absorption coefficient of the sample material can be obtained. However, determining these electromagnetic parameters should be performed cautiously when samples are more or less transparent. In this chapter, we explain how to extract the material parameters from terahertz time-domain data. We list the main sources of error, and their contribution to uncertainties. We give rules to select the most adapted technique for an optimized characterization, depending on the transparency of the samples, and address the case of samples with strong absorption peaks or exhibiting scattering.

Keywords: terahertz time-domain spectroscopy, transmission TDS, reflection TDS, attenuated total reflection, extraction precision, Kramers-Kronig relations, scattering

1. Introduction

Up to the end of the 1980s, the far-infrared electromagnetic response of materials was mostly investigated thanks to Fourier transform infrared (FTIR) spectroscopy, which exhibits several advantages. During one scan, the recorded time-equivalent waveform is built from information delivered by the entire spectrum, whereas other dispersive prism- or grating-based spectrometers receive at any time only signal from a narrow band, i.e., a weaker signal with a smaller signal-over-noise ratio (SNR). Second, and oppositely to dispersive spectrometers,

the resolution of FTIR instruments is not limited by the size of the source. These are respectively known as the multiplex and *étendue* advantages [1]. Nevertheless, FTIR instruments display some drawbacks mostly due to the lack of efficient sources and detectors of far-infrared waves. The sources must be broadband in view of achieving narrow waveforms and thus performing broad spectral measurements. Generally, blackbody-like sources are implemented: they are rather powerless and deliver incoherent light. Thus, a long integration time is necessary to get a high SNR. Moreover, to obtain a high-frequency resolution, the waveform must be recorded over a long equivalent time window, during which noise is also recorded. Sensitive detectors, like Si bolometers, operate only at cryogenic temperatures. These experimental problems, i.e., long recording times and cryogenic temperature, were solved by Auston and Chueng [2] in 1985 who introduced and demonstrated the new concept of coherent time-domain far-infrared spectroscopy, known today as terahertz time-domain spectroscopy (THz-TDS). This initial work was completed by researchers at IBM Corp. [3, 4], who definitively installed THz-TDS as a very competing tool to study the far-infrared properties of materials and devices. Since these pioneering researches, a strong effort has been devoted by numerous laboratories worldwide to improve THz-TDS equipment and techniques. Today, several books describe this technology [5–9] and commercial systems are available [10]. THz-TDS typically permits to investigate the range 0.1–5 THz, but some recent systems allow one to reach the mid-infrared, i.e., frequencies larger than 10 THz [11–13]. In addition, the time-domain technique makes possible to perform optical-pump and THz-probe time-resolved experiment to study the carrier dynamics in semiconductors [14, 15] or the kinetics of photo-induced chemical reactions [16, 17]. Moreover, nonlinear THz effects can be observed, thanks to the huge THz peak power in THz-TDS systems fed by amplified mode-locked lasers [18].

In this chapter, we describe the principles of THz-TDS and we explain how to extract the refractive index and the coefficient of absorption of materials from THz-TDS data. We study the precision of this determination versus different error sources. We give rules to choose, depending on the samples under test, the most adapted THz-TDS technique among transmission or reflection ones. We also treat the case of materials that exhibit strong absorption bands, and heterogeneous materials that scatter and/or diffract the THz beam.

2. Principles and basics of THz-TDS

In THz-TDS setups, a train of ultra-short laser pulses excites a THz antenna, which converts each optical pulse into an electromagnetic (EM) burst and radiates it in free space. In other words, the carrier frequency of the optical pulse is rectified and only its envelope is saved. Because of a noninstantaneous response of the antenna, the conversion widens the EM pulse duration when compared to the optical one. Thanks to some THz optical system, the EM pulse is focused onto a receiving THz antenna, which is triggered by a delayed part of the laser beam. In the receiving antenna, a nonlinear process mixes both incoming EM pulse and laser pulse, giving rise to a signal integrated by the reading electronics, which is proportional

http://dx.doi.org/10.5772/66348

to the convolution product of the laser pulse and the electrical field of the EM pulse. By varying the time delay between emission and detection, which corresponds to a time-equivalent sampling, the temporal waveform of the convolution product is obtained. Two major features should be noted: (i) emitter and receiver are enlightened by the same pulsed laser beam, thus they are perfectly synchronously excited; and (ii) because it is triggered by ultra-short laser pulses, the receiver records the EM pulse signal only when it is excited by the laser pulses (typically during a 1-ps time slot): noise in the time interval between two consecutive laser pulses (typically 10 ns) is not recorded. This amazing 1 ps/10 ns = 10^4 ratio, associated with the perfect synchronization between emission and detection, together with the high stability of mode-locked laser pulse comb, makes the dynamics of THz-TDS extremely high, usually larger than 60 dB in power. The spectrum of the signal is calculated through a numerical Fourier transform of the convolution trace. The Fourier transform supplies a complex value, with a modulus and a phase. The phase is related, in the time domain, to the relative origin of the time delay between emission and detection while the modulus spectrum depends strongly on (i) the spectral efficiency of the emitting and receiving THz antennas, and (ii) the adjustment of the quasi-optical THz-TDS system. The most common THz antennas are photo-conducting switches made from ultrafast semi-insulating semiconductors, like low-temperature grown GaAs (LTG-GaAs). Basically, a microstrip line with a narrower gap at its center is deposited over the semiconductor substrate. In emission, the structure is DC biased and the gap becomes conductive when illuminated by a laser pulse. It behaves as a dipole whose moment varies promptly due to the photoconduction process. This dipole radiates in the far-field region an EM signal proportional to the second time-derivative of the moment variation, i.e., to the first derivative of the current (conduction and displacement) surge flowing through the gap. In such antennas, detection occurs through a complementary effect. The gap is biased by the incoming THz field $E(t)$ that accelerates the free carriers synchronously generated by the triggering laser pulses. This current, proportional to the THz field, is read and time-integrated by the electronics, usually a lock-in amplifier and it writes:

$$S(\tau) \propto \int_{-\infty}^{+\infty} E(t)N(t-\tau)\,dt, \tag{1}$$

where τ is the time delay between emission and detection, and $N(t-\tau)$ is the number of photocarriers resting at time t from a generation occurring a delay τ before. The spectrum of $S(\tau)$ is obtained by a Fourier transform of Eq. (1):

$$\tilde{S}(\omega) = \mathrm{TF}[S(\tau)] \propto \int_{-\infty}^{+\infty}\int_{-\infty}^{+\infty} E(t)N(t-\tau)e^{-j\omega\tau}\,dt\,d\tau \propto \tilde{E}(\omega)\tilde{N}^{*}(\omega) \tag{2}$$

ω is the angular frequency, $\tilde{E}(\omega)$ and $\tilde{N}(\omega)$ are the spectra of $E(t)$ and $N(t)$, and $\tilde{N}^{*}(\omega)$ is the complex conjugate of $\tilde{N}(\omega)$. From now on, a tilde denotes a complex variable.

THz emission can also be obtained either by illuminating the bare surface of an ultrafast semiconductor wafer, at which photo-generated carriers are accelerated inside the wafer by surface fields or/and by the Dember effect [19], or by optical rectification in an electro-optic (EO) crystal effect. Detection is also commonly performed by EO sampling. Characterization of a sample is mostly achieved in transmission by locating the sample in the THz beam, and recording the THz waveforms without (reference) and with the sample. Then, one Fourier

transforms the waveforms, and the complex transmission coefficient $\tilde{T}_{meas}(\omega)$ of the sample is equal to the ratio of the signal and reference spectra:

$$\tilde{T}_{meas}(\omega) = \frac{\tilde{S}(\omega)}{\tilde{S}_{ref}(\omega)} = \frac{\tilde{E}(\omega)\tilde{N}^*(\omega)}{\tilde{E}_{ref}(\omega)\tilde{N}^*(\omega)} = \frac{\tilde{E}(\omega)}{\tilde{E}_{ref}(\omega)}. \quad (3)$$

The same procedure is performed in reflection, providing the experimental complex coefficient of reflection $\tilde{R}_{meas}(\omega)$. In this case, the reference signal is the THz waveform reflected by a perfect mirror placed exactly at the same position as the sample to be tested. To avoid the difficulty of the exact positioning of the reference mirror, attenuated total reflection (ATR) scheme is preferred [20]. ATR set-ups are especially dedicated to characterize liquids or powders since (i) THz radiations are strongly absorbed by classical liquids like water avoiding any transmission measurement, and (ii) ATR scheme is sensitive enough to characterize dilutions whose solute concentration could be as small as 1%. In ATR experiment, the THz beam is reflected against the base of a prism whose index of refraction is higher than that of the studied substance to achieve total internal reflection of the THz beam. The reference is recorded without the material placed upon the prism base to finally obtain the measured complex total reflection coefficient $\tilde{R}_{ATR,meas}(\omega)$.

The complex refractive index $\tilde{n} = n(\omega) + j\kappa(\omega)$ of the sample to be characterized is determined when the calculated transfer function (i.e., either $\tilde{T}(\omega,\tilde{n})$, $\tilde{R}(\omega,\tilde{n})$, or $\tilde{R}_{ATR}(\omega,\tilde{n})$), in which $\tilde{n}$ is the only adjustable variable, is equal to the experimental ones ($\tilde{T}_{meas}(\omega)$, $\tilde{R}_{meas}(\omega)$, or $\tilde{R}_{ATR,meas}(\omega)$, respectively). When dealing with nonmagnetic materials, analytical expressions of the transfer functions are rather simple as long as the samples are slabs with parallel and flat faces. At the sample location, the incoming THz beam must be a plane wave. In practice, this is verified even with focused THz Gaussian beams, as far as the sample, placed at the focal point, is thinner than the Rayleigh length of the beam. Thus, analytical expressions of $\tilde{T}(\omega,\tilde{n})$, $\tilde{R}(\omega,\tilde{n})$, and $\tilde{R}_{ATR}(\omega,\tilde{n})$ are as follows:

$$\tilde{T}(\omega,\tilde{n}) = \frac{4\tilde{K}}{(\tilde{K}+1)^2}\phi^{-1}FP(\omega,\tilde{n})e^{-j\frac{\omega}{c}\cos\theta\, d} \quad (4)$$

$$\tilde{R}(\omega,\tilde{n}) = \pm\frac{1-\tilde{K}}{1+\tilde{K}}\left(1-\phi^{-2}\right)FP(\omega,\tilde{n}),\ \ \tilde{R}_{ATR}(\omega,\tilde{n}) = \pm\frac{1-\tilde{K}}{1+\tilde{K}} \quad (5)$$

with $\tilde{K}_{TE} = \tilde{n}^2\,\tilde{K}_{TM} = \frac{\sqrt{\tilde{n}^2-\sin^2\theta}}{\cos\theta}$, $\phi = e^{j\frac{\omega}{c}d\sqrt{\tilde{n}^2-\sin^2\theta}}$, and $FP(\omega,\tilde{n}) = \left[1-\left(\frac{\tilde{K}-1}{\tilde{K}+1}\right)^2\phi^2\right]^{-1}$.

θ is the angle of incidence, d is the sample thickness, and c the speed of the light in vacuum. In Eq. (5), the sign "+" is for the TE polarization case and "-" for the TM one. In the ATR case, $\tilde{K}$ takes similar expressions in which $\tilde{n}$ is substituted by $\tilde{n}/n_p$, where n_p is the refractive index of the prism. $FP(\omega,\tilde{n})$ is the Fabry-Perot term that accounts for the rebounds of the THz pulse in the sample. In ATR experiments, we suppose that d is much larger than the evanescent length of the THz beam in the sample, so rebounds are neglected as well as in reflection when the sample is opaque or strongly absorbing. In this case, for both reflection and ATR cases, solving $\tilde{R}(\omega,\tilde{n}) = \tilde{R}_{meas}(\omega)$ is easy because Eq. (5) can be analytically inversed:

$$\tilde{K} = \frac{1\pm\tilde{R}(\omega,\ \tilde{n})}{1\mp\tilde{R}(\omega,\ \tilde{n})} \quad (6)$$

Solving Eq. (4) (or Eq. (5) for thin samples) is more difficult because of the oscillatory complex exponential term ϕ. Consequently, the modulus and phase of $\tilde{T}(\omega,\tilde{n})$ or $\tilde{R}(\omega,\tilde{n})$ plotted in function of n and κ exhibit several minima (see **Figure 1**). Therefore, finding the right zero of $\tilde{T}(\omega,\tilde{n}) = \tilde{T}_{meas}(\omega)$ or $\tilde{R}(\omega,\tilde{n}) = \tilde{R}_{meas}(\omega)$ is not an easy task.

http://dx.doi.org/10.5772/66348

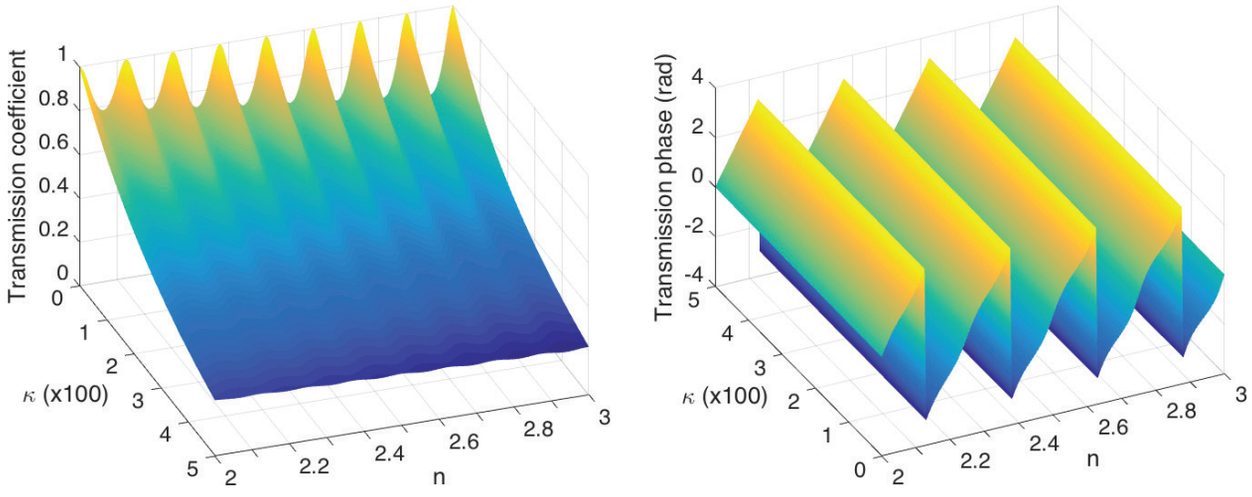

Figure 1. Map of the modulus (left) and the wrapped phase (right) of $\tilde{T}(\omega, \tilde{n})$ versus n and κ. The sample is 1.2-mm thick and the frequency is 1 THz.

To get rid of the oscillatory behavior, we proposed [21] to employ an error function $\delta(\omega, \tilde{n})$ that exhibits a monotonous shape with a single minimum that is quickly found with any numerical method:

$$\delta(\omega, \tilde{n}) = \left[\ln(|\tilde{X}(\omega, \tilde{n})|) - \ln\left(\left|\tilde{X}_{\text{meas}}(\omega)\right|\right)\right]^2 + \left[\arg(\tilde{X}(\omega, \tilde{n})) - \arg\left(\tilde{X}_{\text{meas}}(\omega)\right)\right]^2 \quad (7)$$

with $\tilde{X} = \tilde{T}$ or $\tilde{R}$. **Figure 2** shows $\delta(\omega, \tilde{n})$ in transmission versus n and κ for two different cases: (i) transmission modulus $T_{\text{meas}} = 0.01$, phase $\varphi_{T,\text{meas}} = 10$ rad, $\omega d/c = 3$ (e.g., a 180-μm thick sample studied at $f = 0.8$ THz), (ii) $T_{\text{meas}} = 0.003$, $\varphi_{T,\text{meas}} = 30$ rad, $\omega d/c = 30$ (e.g., a 2.4-mm thick sample studied at $f = 0.6$ THz). A single zero of $\delta(\omega, \tilde{n})$ is clearly seen, at which n and κ can be almost instantaneously extracted using a numerical routine.

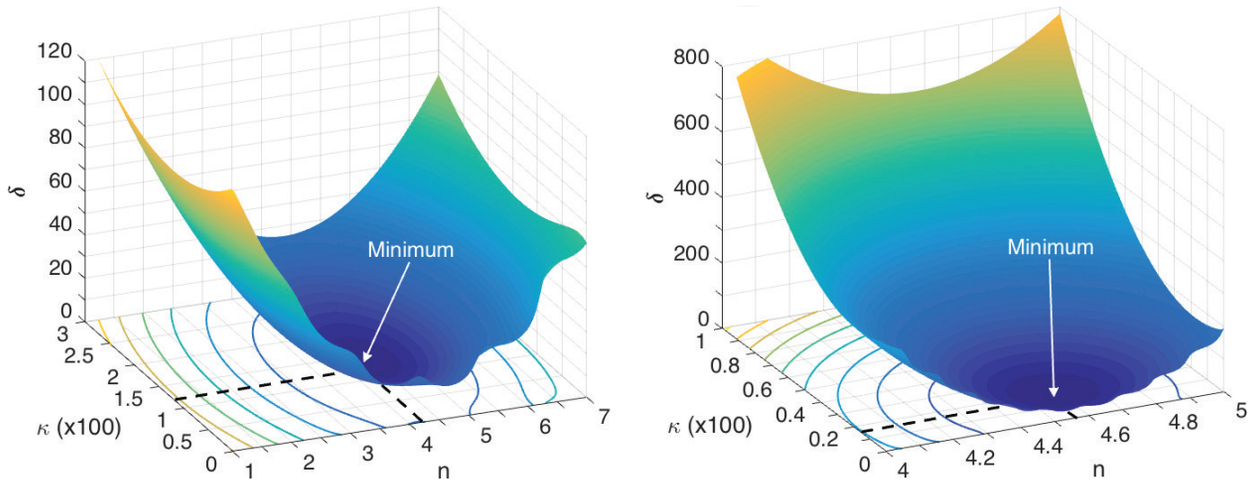

Figure 2. Maps of the error function δ versus n and κ, with T meas = 0.01, φ T,meas = 10 rad, $\omega d/c = 3$ (left), and T meas = 0.003, φ T,meas = 30 rad, $\omega d/c = 30$ (right).

3. Precision on the parameters determination

The material parameters (n and κ) determined by THz-TDS are obtained with a precision that is limited [22] by (i) a bad knowledge of the sample parameters (erroneous thickness, not parallel sides, surface roughness, inhomogeneity, etc.), (ii) a bad positioning of the sample, (iii) the fact that the THz beam is not a plane wave, and (iv) the experimental noise. Also, one must take into account errors and noises arising from a deficient delay line (mechanical drift, registration, etc.). In Ref. [22], Withayachumnankul et al. have given a complete study of the causes of uncertainty in THz-TDS in terms of variance of the recorded signals. Here our approach is simplified but leads to analytical expressions, which emphasize the role and the weight of each experimental parameter.

3.1. Effect of a bad value of the sample thickness

A bad value of the thickness d modifies the results in the case of transmission THz-TDS. The induced error Δn is calculated by setting the differential of $\tilde{T}(\omega, \tilde{n})$ equal to zero. We get:

$$\Delta\tilde{n} = \Delta d \frac{\partial \tilde{T}}{\partial d} / \frac{\partial \tilde{T}}{\partial \tilde{n}} \tag{8}$$

Let us suppose, for the sake of sim and reflection are obtained by differentiating plification, that the Fabry-Perot rebounds can be removed by a proper time-windowing of the THz waveform. Thus, Eq. (4) of $\tilde{T}(\omega, \tilde{n})$ becomes:

$$\tilde{T}(\omega, \tilde{n}) \approx \frac{4\tilde{K}}{(\tilde{K}+1)^2} e^{j\frac{\omega}{c}\left(\cos\theta - \sqrt{\tilde{n}^2 - \sin^2\theta}\right)d} \tag{9}$$

A simple calculation leads to:

$$\Delta\tilde{n}_{TE} = \frac{j\frac{\omega}{c\tilde{n}}(\tilde{X}-\cos\theta)\tilde{X}^2}{\frac{\tilde{X}-\cos\theta}{\tilde{X}+\cos\theta} + j\tilde{X}\frac{\omega}{c}d}\Delta d, \quad \Delta\tilde{n}_{TM} = \frac{j\frac{\omega}{c\tilde{n}}(\tilde{X}-\cos\theta)\tilde{X}^2}{\frac{\tilde{X}-\tilde{n}^2\cos\theta}{\tilde{X}+\tilde{n}^2\cos\theta}\left(1-2\frac{\tilde{X}^2}{\tilde{n}^2}\right) + j\tilde{X}\frac{\omega}{c}d} \tag{10}$$

with $\tilde{X} = \sqrt{\tilde{n}^2 - \sin^2\theta}$. Usually, experiments are performed at normal incidence, for which Eq. (10) simplifies into:

$$\Delta\tilde{n} = j\frac{\omega}{c}\frac{\tilde{n}-1}{\frac{\tilde{n}-1}{\tilde{n}+1} + j\frac{\omega}{c}\tilde{n}d}\Delta d. \tag{11}$$

Typically, an error of 1% on d leads to an error smaller than 1% on n and κ (see **Figure 3**).

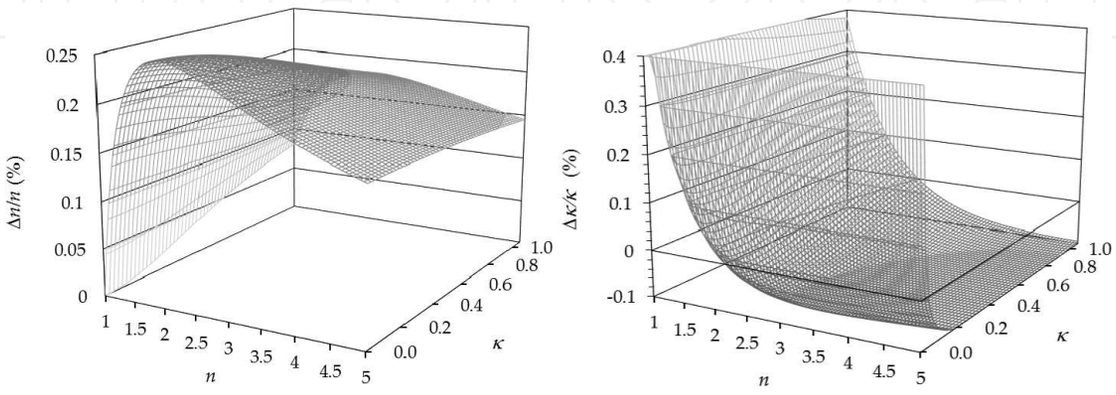

Figure 3. Δn (left) and $\Delta\kappa$ (right) in %, versus n and κ, induced by a Δd =10 μm thickness error. The sample is 1-mm thick ($\Delta d/d$= 1%) and f = 1 THz.

http://dx.doi.org/10.5772/66348

3.2. Effect of an angular tilt

Using the same procedure, we investigate the influence of a bad orientation of the sample. The derivation is done versus the tilt angle $\Delta\theta$. Under normal incidence, we get in transmission:

$$\Delta\tilde{n}_{TE} = \frac{j\frac{\omega}{c}\tilde{n}\,d}{\frac{\tilde{n}-1}{\tilde{n}+1}+j\frac{\omega}{c}d}\Delta\theta, \Delta\tilde{n}_{TM} = \frac{j\frac{\omega}{c}\tilde{n}\,d}{\frac{\tilde{n}-1}{\tilde{n}+1}+j\frac{\omega}{c}\tilde{n}d}\Delta\theta. \quad (12)$$

A slight difference is obtained if the angular tilt is along the direction of the E-field (TE) or perpendicular to it (TM). As shown in **Figure 4**, an angular tilt of 1° induces typically an error Δn much smaller than 1%, except for small values of n and κ, for which the error is of the order of 1%. However, as imaging the THz-TDS beam is almost impossible, adjusting precisely the orientation of the sample in the beam is a difficult task and angular error tilts of several degrees are possible, which leads to errors larger than 1%.

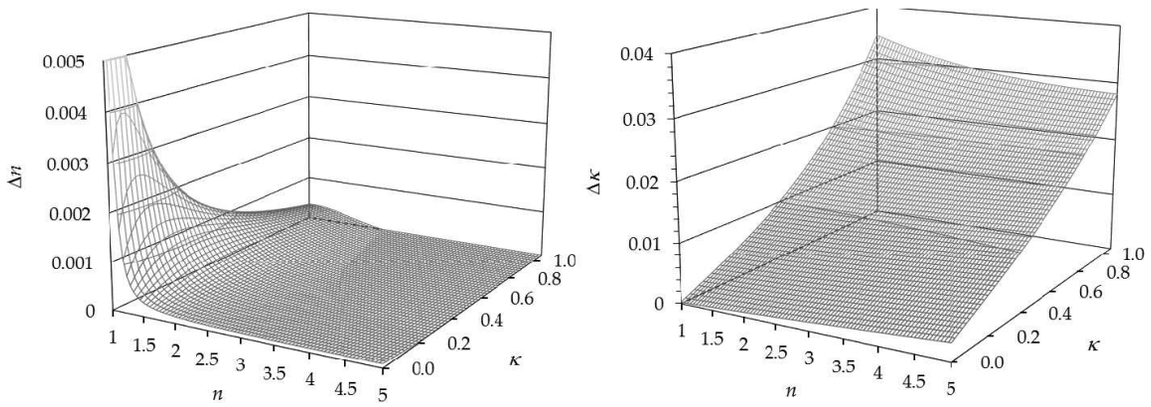

Figure 4. Δn (left) and $\Delta\kappa$ (right), versus n and κ, induced by a $\Delta\theta = 1°$ tilt in TE polarization. The sample is 1-mm thick and $f = 1$ THz.

Even if the samples are perfectly well aligned relatively to the THz propagation axis, a non-collimated THz beam could lead to inaccuracies equivalent to those induced by angular tilt. Indeed, any converging Gaussian beam can be decomposed into plane waves arriving onto the sample under different incidence angles, from 0° (along the propagation axis) up to the diffraction angle whose value depends on the frequency. Referring to **Figure 4**, this could induce an error of about 1%. This unwanted effect gets even worse as THz converging Gaussian beam probes thick samples, because it defocuses the THz beam that impinges the receiver. Consequently, the detected signal can be respectively larger or weaker than expected, which leads to an over- or underestimation of the sample losses.

In reflection, a bad orientation (angular tilt $\Delta\theta$) of the tested sample leads to an additional error given by:

$$\Delta\tilde{n}_{TE} = \Delta\tilde{n}_{TM} = \frac{\tilde{n}^2-1}{2\tilde{n}}(\Delta\theta)^2 \quad (13)$$

By comparing expressions (12)—transmission—and (13)—reflection—it appears that the error Δn induced by an angular tilt is weaker (typ. 1/1000) in reflection than in transmission: this is due to the additional path of propagation in the material induced by the tilt in the

transmission scheme, while the effect on the Fresnel coefficients at the sample interfaces is smaller. Nevertheless, it should be noticed that an angular tilt, in reflection THz-TDS, is more perturbing, as all the energy of the deviated THz beam may not reach the detector. This error, which depends on each set-up design, could be quite large in reflection THz-TDS, but it could be wiped out by carefully aligning the set-up and the sample.

3.3. Effect of a bad positioning of the reference mirror in reflection THz-TDS

In the case of reflection THz-TDS, the main geometrical error source is the misalignment of the sample as compared to the reference mirror. For the sake of simplicity, we suppose that the sample is thick enough to neglect the Fabry-Perot rebounds. Let δ be the difference in position, which induces an erroneous phase difference $2\delta\,\omega/c$:

$$\tilde{R}_{\text{meas}}(\omega,\tilde{n}) \;=\; \tilde{R}(\omega,\tilde{n})\;\; e^{j2\frac{\omega}{c}\delta} \;=\; \frac{\tilde{n}-1}{\tilde{n}+1}\,e^{j2\frac{\omega}{c}\delta} \;=\; \tilde{R}(\omega,\tilde{n}+\Delta\tilde{n}) \;=\; \frac{\tilde{n}+\Delta\tilde{n}-1}{\tilde{n}+\Delta\tilde{n}+1} \tag{14}$$

This phase difference leads to an error $\Delta\tilde{n}$:

$$\Delta\tilde{n} \;\approx\; j2\,\frac{\omega}{c}(\tilde{n}^2-1)\delta \tag{15}$$

Because of the j term, the error Δn depends on the imaginary part of $\tilde{n}^2$, i.e., it is proportional to $n\kappa$. For transparent materials ($\kappa \approx 0$), the error is negligible, but it becomes large for opaque materials that are usually characterized in reflection THz-TDS. The error $\Delta\kappa$ that varies as $n^2-\kappa^2$ is small for opaque materials and large for transparent materials. Therefore, THz-TDS in reflection is a well-adapted and precise technique for the determination of the absorption of opaque materials. **Figure 5** shows the effect of a 1-μm position shift versus n and α at $f = 1$ THz. The error Δn is of the order of a few percent, while the error $\Delta\alpha$ is larger especially for transparent materials ($\Delta\alpha$ ~100 cm^{-1} for $n = 2.6$).

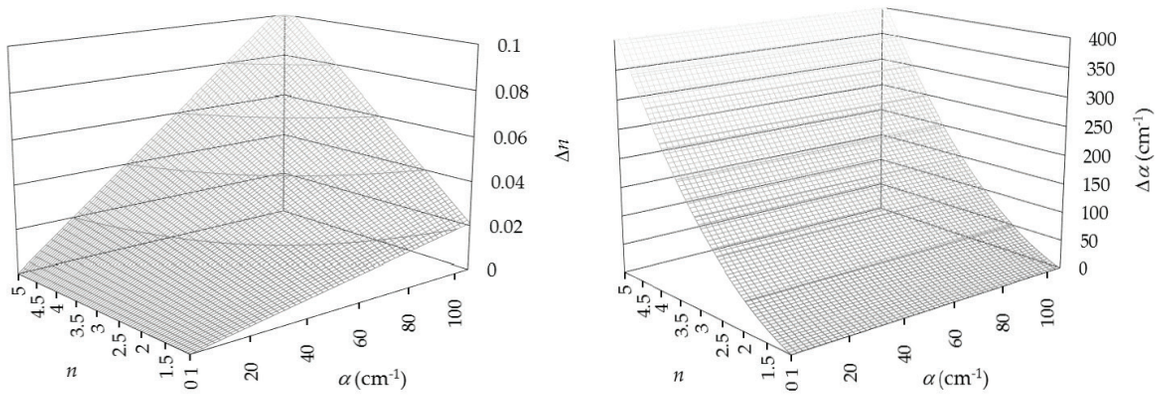

Figure 5. Δn (left) and $\Delta\alpha$ (right), versus n and α, induced by a $\delta = 1$-μm shift of the mirror position in reflection THz-TDS for $f = 1$ THz.

These rather large errors are induced by very small shifts, here $\delta = \lambda/300$, and get even larger at higher frequencies, according to Eq. (15). Therefore, in reflection THz-TDS, a great attention must be paid to position the sample at the exact location of the reference mirror, or, if not

http://dx.doi.org/10.5772/66348

possible, to either control, measure, or correct the induced phase difference. For that purpose, it exists several experimental [23–26] or numerical [27] solutions.

3.4. Effect of a noise with photo-conducting THz antennas

Noise makes uncertain the measured values of the magnitude and the phase of the THz signals. Let us treat here only the case of photo-conducting antennas. We call σ^2 the noise power, i.e., the square of the variance of the THz signals. A first noise σ_E^2 is generated by the emitter: shot noise due to the random arrival of the pump laser photons, fluctuation of the laser intensity, etc. Drift and mechanical vibrations of the optical delay line as well as random fluctuations of the laser beam direction add a noise-equivalent contribution. It depends strongly on the equipment: Withayachumnankul et al. [22] have measured an amplitude variance of the order of 10^{-3} that was mostly due to delay-line registration and mechanical drift. This noise is of the same order as σ_E^2 defined previously and can be included in the emitter noise. The THz beam, together with its noise, is then reflected or transmitted by/through the sample toward the receiving antenna. At the receiver, two additional noises perturb the recorded signal, namely, the shot noise σ_{sh}^2 that is proportional to the recorded current S_{meas} ($\sigma_{sh}^2 = 2e\Delta f\, S_{\text{meas}}$, Δf is the detection bandwidth and e the electron charge), and a noise σ_D^2 that is independent of the current (Johnson noise, amplification noise, thermal noise, etc.). The total noise is the sum of all these contributions:

$$\sigma^2 = \left|\frac{S_D}{S_E}\right|^2 \sigma_E^2 + 2e\,\Delta f\, S_D + \sigma_D^2, \tag{16}$$

where S_E is the current recorded without sample in the set up (reference current), whereas S_D is the current recorded with the sample. Taking into account the small value of the noise when compared to the signal (perturbation approach), we get:

$$\sigma_X^2 = A(\omega)X^2 + B(\omega)X + C(\omega). \tag{17}$$

Here, X is the modulus of the complex coefficients of reflection $\tilde{R}$ or transmission $\tilde{T}$, depending on the type of performed THz-TDS measurements. A, B, and C are parameters specific to each THz-TDS set-up and are given by:

$$A(\omega) = \frac{2\,\sigma_E^2 + 2e\,\Delta f\,|S_E| + \sigma_D^2}{|S_E|^2}, \quad B(\omega) = \frac{2e\,\Delta f}{|S_E|}, \quad C(\omega) = \frac{2e\,\Delta f\,\sigma_D^2}{|S_E|^2} \tag{18}$$

Figure 6 shows the A, B, and C coefficients of our homemade THz-TDS set up, built around a mode-locked laser (Tsunami Spectra-Physics, 50 fs pulse duration at the antennas, 82 MHz repetition rate, pumped with a CW Millenia laser) and LTG-GaAs dipole-like THz antennas. The coefficients were determined as follows. Several samples of different thicknesses, and thus of different transmission coefficients, were made from the same material (Stycast glue). For each sample, several transmission THz-TDS data were recorded, and the noise was deduced from the standard deviation of the transmission spectra. Then, the noise was plotted at any given frequency as a function of T and fitted with expression (17). Typically, at the maximum of sensitivity of the LTG-GaAs antennas, i.e., around 0.5 THz, $A \approx 15 \times B \approx 200 \times C$. It follows that the main source term is the noise in the emitter (σ_E^2), which is larger than the noise in the detector (σ_D^2). As the main difference in receiving and emitting antennas is the photocurrent (both antennas are similar and excited by the same laser power), we conclude that the optical shot noise and laser intensity fluctuations in the emitter are the major source of noise.

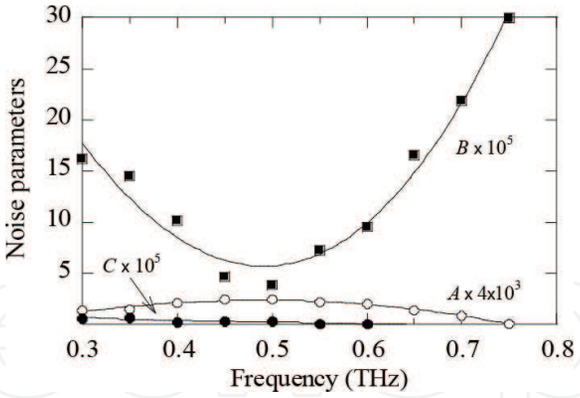

Figure 6. *A*, *B*, and *C* (SI unit) coefficients experimentally determined from transmission THz-TDS of several samples of Stycast having different thicknesses. The data have been recorded with a THz-TDS system equipped with LT-GaAs antennas. The lines are a guide to the eye.

Relations (17) and (18) indicate that the standard deviation is proportional to the detection bandwidth Δf. Thus, reducing Δf, i.e., increasing the integration time of a lock-in amplifier, decreases the error as well. On the other hand, the *A*, *B*, and *C* coefficients vary inversely to the available incoming THz signal. Increasing the THz power of the emitting antenna reduces the uncertainties. The influence of noise on the measurement precision is derived as follows. One writes any experimental spectral component, in terms of magnitude and phase, as the sum of the actual value and noise:

$$\tilde{X}_{\text{meas}}(\omega,\tilde{n}) = X_{\text{meas}}\ e^{j\varphi_{\text{meas}}} = X\ e^{j\varphi} + X_{\text{noise}}\ e^{j\varphi_{\text{noise}}} \tag{19}$$

Assuming the noise is much smaller than the signal, one easily gets:

$$X_{\text{meas}} = X + \cos\left(\varphi - \varphi_{\text{noise}}\right)X_{\text{noise}}, \qquad \tan\varphi_{\text{meas}} = \frac{X\sin\varphi + X_{\text{noise}}\sin\varphi_{\text{noise}}}{X\cos\varphi + X_{\text{noise}}\cos\varphi_{\text{noise}}} \tag{20}$$

With a fully random phase noise, the related standard deviations of the modulus and phase of the measured signals are:

$$\sigma_X = \overline{\left(X_{\text{meas}} - X\right)^2}^{1/2} = \sqrt{\frac{1}{2}\overline{X^2_{\text{noise}}}}, \qquad \sigma_\varphi = \frac{\sigma_X}{X}. \tag{21}$$

The validity of our analysis is experimentally verified as depicted in **Figure 7**. The standard deviations of the modulus *R* and phase φ of the signal reflected by a HR-Si wafer is plotted versus frequency. The dashed lines represent the standard deviation as obtained from averaging eight different measures, whereas the continuous lines are calculated with Eq. (21). Between 0.2 and 1.2 THz, SNR is large and the agreement between calculation and experiment is good. Outside this range, the noise is too large and thus our perturbation approach is no more valid.

Finally, one should derive the experimental standard deviation from the actual measured signals. The *X* value is the ratio of the transmitted or reflected signal S_X over reference signal S_{Ref}:

$$X_{\text{meas}} = \frac{S_X + S_{X,\text{noise}}}{S_{\text{Ref}} + S_{\text{Ref,noise}}} \approx X + \frac{S_{X,\text{noise}} - X\ S_{\text{Ref,noise}}}{S_{\text{Ref}}}. \tag{22}$$

The standard deviation is calculated from Eq. (22):

$$\sigma_X^2 = \frac{\sigma_X^2 + X^2\ \sigma_{\text{Ref}}^2}{S_{\text{Ref}}^2} \tag{23}$$

http://dx.doi.org/10.5772/66348

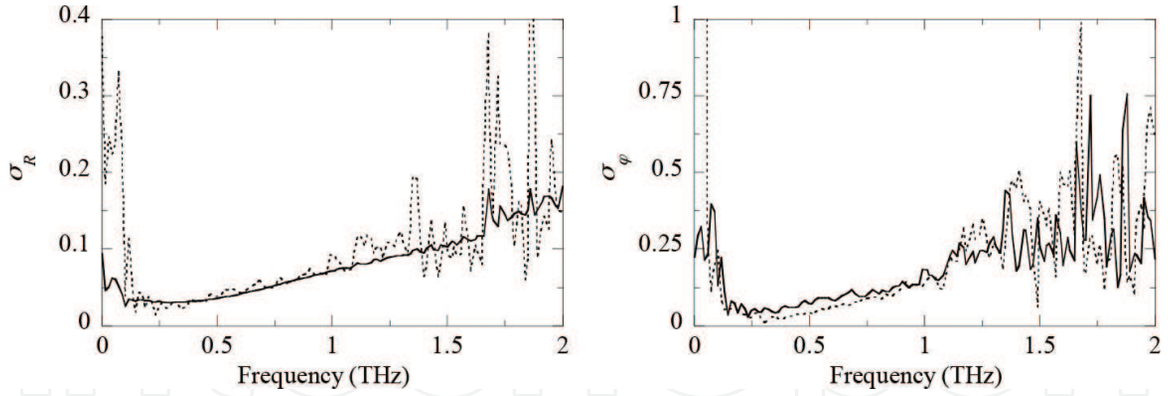

Figure 7. Standard deviations σ_R and σ_φ versus frequency for the THz signal reflected by a HR-Si wafer. The dashed line is obtained from eight different measurements, whereas the continuous line is calculated.

The noise-induced errors Δn_{T_R} and $\Delta \kappa_{T_R}$ in transmission and reflection are obtained by differentiating Eq. (4) or Eq. (5), respectively. In the general case of oblique incidence, the differential expressions are huge and complicated but get simpler in the case of normal incidence, when rebounds can be filtered. In this latter case one obtains:

$$\Delta n_T \simeq (1+n)^3 \frac{n\beta(1+n)+n-1}{(n-1)^2+n^2\beta^2(1+n)^2} e^{\kappa\beta} \frac{\sigma_T}{4}, \quad \Delta \kappa_T \simeq \frac{\beta(1+n)-n+1}{n\beta(1+n)+n-1} \Delta n_T \tag{24}$$

$$\Delta n_R = \Delta \kappa_R = 2\frac{\left|(1+R^2)\cos\varphi - 2R\right| + \left|\sin\varphi\right|(1-R^2)}{\left(1-2R\cos\varphi+R^2\right)^2}\sigma_R. \tag{25}$$

$\beta = \frac{\omega d}{c}$. Examples of so-determined error Δn_{T_R} are presented in **Figure 8**. For the Stycast samples, THz-TDS experiments performed in transmission leads to the amazing precision $\Delta nT/n < 0.05\%$ between 0.6 and 1 THz. However, this value is only the noise-induced error and the actual total imprecision (~1%) is mainly due to a bad position of the sample or a bad knowledge of the sample thickness, as explained above. Conversely, characterizing HR-Si in reflection is definitively not the best way, as the uncertainty is never below 10%. We explain below how to choose the optimized THz-TDS technique in order to get a more precise determination of the material parameters. In the case of oblique incidence and of ATR measurements, one cannot get analytical expressions like Eqs. (24) and (25), and thus the errors should be numerically estimated.

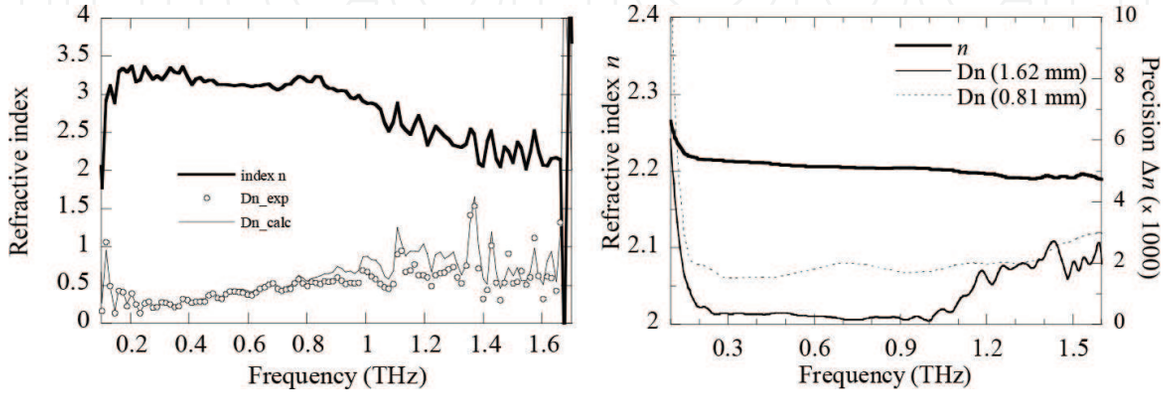

Figure 8. Spectra $n(f)$ together with the error $\Delta n(f)$; left: HR-Si measured in reflection. Continuous line and open circles are calculated using Eq. (25) in which σ_R is estimated using expression (17) with A, B and C given in Figure 6, and measured, respectively; right: Stycast measured in transmission (sample thickness 0.81 and 1.62 mm).

Figure 9 summarizes the influence for the different error sources in transmission THz-TDS. The sample is a 1-mm thick slab, with $n = 2$ and $\kappa = 0.01$. The errors Δn and $\Delta\kappa$ are plotted versus frequency in the case of a thickness error $\Delta d = 0.01$ mm, of an angular tilt $\Delta\theta = 1°$, and a noise defined by Eq. (24) in which σT is substituted by expression (17) with $A = 10^{-3}$, $B = 10^{-5}$, and $C = 10^{-6}$.

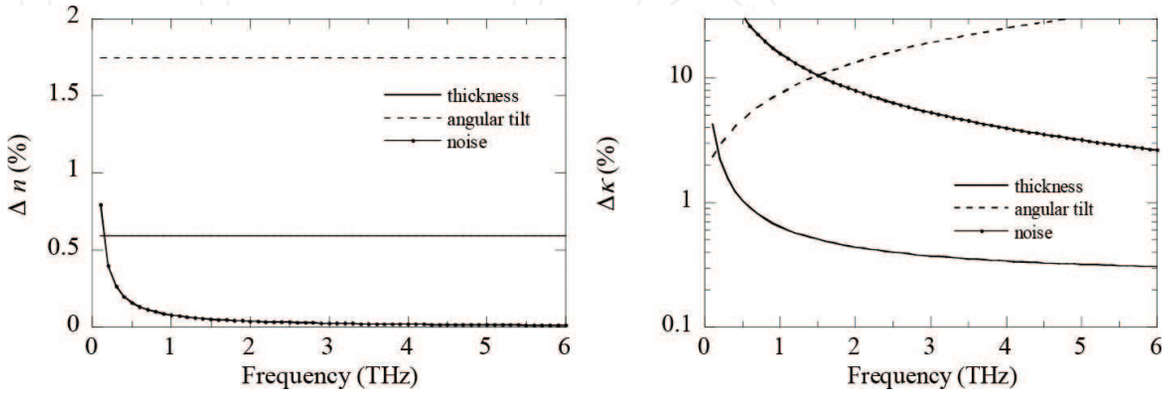

Figure 9. Δn (left) and $\Delta\kappa$ (right) versus frequency as induced by a 1% thickness error (thick continuous line), by a 1° tilt (thin continuous line) and by the noise (dotted line). Thes estimation is made in transmission for a 1-mm thick sample with $n = 2$ and $\kappa = 0.01$.

The angular tilt is by far the largest source of error for the refractive index n. κ is mostly affected by the noise at lower frequencies, while the angular tilt effect is predominant at higher frequencies. In any case, $\Delta\kappa$ is larger than Δn, especially at lower frequencies, where $\Delta\kappa$ in percent tends toward infinity because of the $1/\kappa$ term. The sum of all these errors is typically 1–2% for n and about 10% for κ. Because of the Fourier transform properties, the precision on the frequency is simply related to the recording time window, i.e., in most of THz set ups, to the length of the mechanical delay line. If the THz waveform is recorded over a time window $\Delta\tau$, the frequency resolution is $\Delta f = 1/\Delta\tau$. Common delay lines are 25–50 mm long, thus $\Delta\tau = 150 \sim 300$ ps, and $\Delta f = 3 \sim 6$ GHz. Using longer delay lines [28] to achieve a better frequency resolution is made difficult because of long-term fluctuations of the laser power and possible weak deviations of the direction of the laser beam.

4. Transmission or reflection THz-TDS?

For opaque samples, it is compulsory to perform THz-TDS measurements in reflection because no THz signal is transmitted. For low-index transparent samples, transmission scheme is preferable, as the induced phase variation is integrated over the whole sample length, while the Fresnel phase change in reflection are weaker. For samples with a moderate absorption coefficient, the choice of the best experimental scheme is not obvious. However, the error study presented in the previous paragraph helps in selecting the optimized THz-TDS characterization technique, i.e., either in reflection or in transmission. For the sake of simplicity, we address

http://dx.doi.org/10.5772/66348

here only the case of normal incidence. We suppose that the samples are perfectly placed in the THz beam (no angular tilt) and that the sample thickness is perfectly known. We suppose also that the sample is thick enough to permit a record of only the directly reflected or transmitted THz pulse, by a proper time-windowing of the other rebounds. Thus, the only source of inaccuracy is induced by intrinsic noises, given by relation (18), resulting on the errors expressed by Eqs. (24) and (25), where σx is expressed using Eq. (17). In reflection, Δn and $\Delta\kappa$ do not depend on the phase term $\beta = \omega d/c$, whereas they do in transmission. Indeed, the transmitted THz signal encounters a phase increase due to propagation through the sample. Thus, we perform our numerical study with β as parameter. **Figure 10** (left) shows $\Delta n_R/\Delta n_T$ versus n and κ calculated for $\beta = 20$ and $A = 10^{-3}$, $B = 10^{-5}$, and $C = 10^{-6}$.

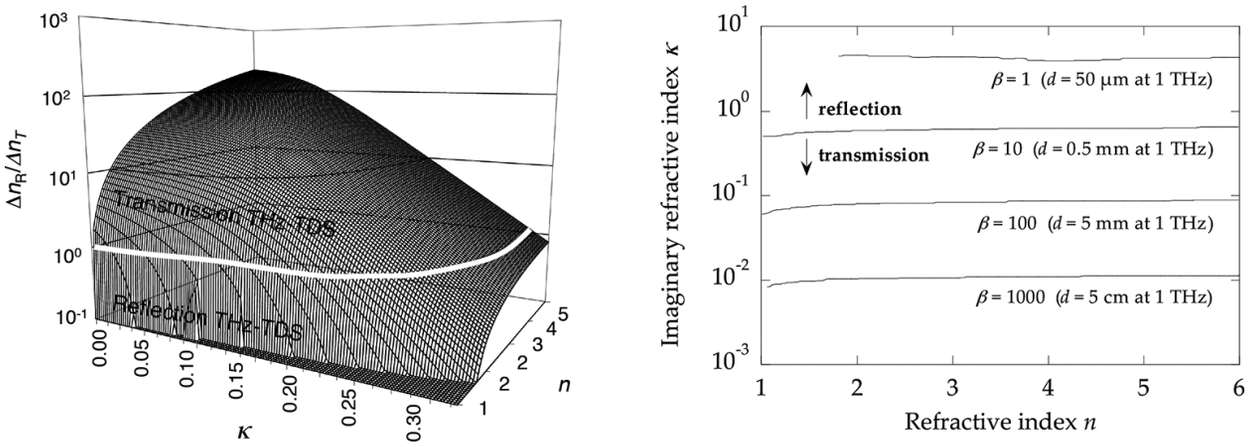

Figure 10. 3D map of the ratio $\Delta n R/\Delta n T$ versus n and κ for $\beta = 20$ (left); limit between the reflection and transmission schemes for an optimized parameter extraction (right).

The white curve indicates the limit $\Delta n_R = \Delta n_T$. Above this limit, $\Delta n_R > \Delta n_T$ and thus transmission TDS is more precise than reflection TDS. This happens when absorption is rather small ($\kappa < 0.3$). At higher absorption, reflection is preferable because the transmitted signal becomes weaker. The limit between both techniques is plotted in the (n,κ) space on **Figure 10** (right) for different β. For a given set-up (given A, B, C values), the technique to be selected depends mostly on κ. For example, a 0.5-mm thick sample studied at 1 THz ($\beta = 10$) should be characterized in transmission as soon as $\kappa < 0.6$, i.e., $\alpha < 12$ cm^{-1}.

5. Combined transmission and reflection THz-TDS

In the far infrared, some materials exhibit strong absorption lines due to molecular resonances or/and due to collective excitations. In gases, narrow molecular resonances correspond to the excitation of mechanical vibrations of the whole molecule structure. In liquids and solid materials, the molecular resonances are coupled and broadened by thermal and density inhomogeneity at the molecular scale, resulting in wider absorption bands. In crystals, excitation of phonons leads also to a strong absorption of the THz waves. When characterizing

such materials in transmission THz-TDS, there could be no signal detected in transmission within the absorption bands. The phase is lost in these spectral regions, and thus extraction of the material parameters at higher frequencies is no more possible using common THz-TDS extraction procedures as $2m\pi$ phase jumps (m is an unknown integer) of the transmitted phase φ_T occur at the absorption peaks. On the other hand, reflection THz-TDS is applicable even in the absorption regions, but its precision is inferior to that of transmission THz-TDS, especially because of a possible shift in position with regards to a reference mirror. Thus, even if R is measured over the whole achievable THz range, the precision Δn_R of the refractive index obtained in reflection THz-TDS is worse than the one Δn_T obtained in transmission, excepted in the absorption bands, as shown in **Figure 11** (left). Both transmission and reflection techniques may be combined to precisely evaluate $\tilde{n}(\omega)$ of such materials over the whole experimental bandwidth [29]. Basically, the procedure consists in determining with a great precision $\tilde{n}_T$ from transmission data in the first region of transparency (below 1.4 THz for maltose, see **Figure 11**, left). Thus, $\tilde{n}_R$ is extracted, with a minor precision, over the whole spectrum from the reflection data. The possible bad position δ of the sample as regards to the reference minor is corrected by adding the necessary frequency-dependent phase term $\Delta \varphi_R = 2\delta\omega/c$, so that $\tilde{n}_R$ equalizes $\tilde{n}_T$ in the first spectral region and thus $\tilde{n}_R$ is corrected over the whole spectrum. In the second region of transparency (1.6–2 THz), the possible $2m\pi$ step of the phase φ_T occurring at the resonance is retrieved by forcing $\tilde{n}_T$ obtained in transmission to be equal to the corrected $\tilde{n}_R$.

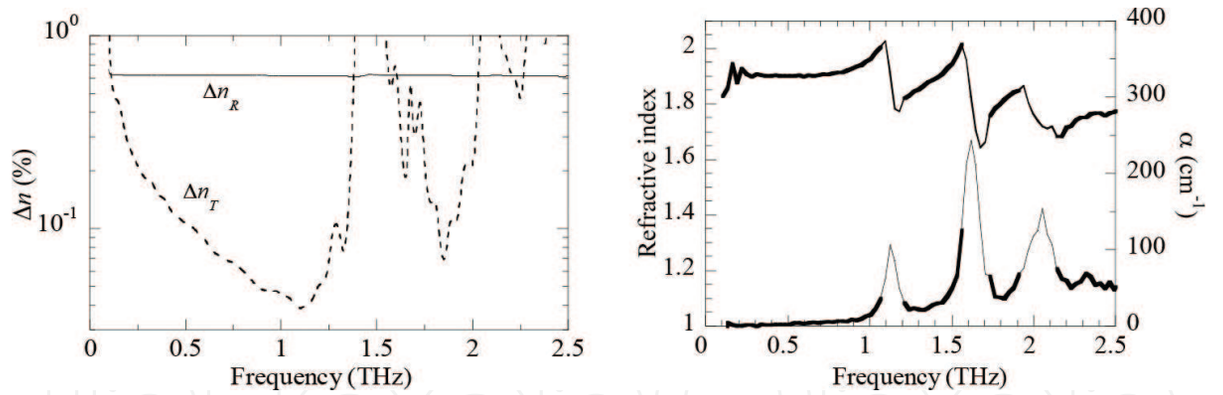

Figure 11. Left: Relative noise-induced error on the refractive index of maltose (2-mm thick) obtained in transmission (Δn_T) and in reflection (Δn_R) THz-TDS. Right: Refractive index n and coefficient of absorption α of maltose, as extracted from THz-TDS measures with an 890-μm thick sample. The thick curves are from corrected transmission data, while the thin ones are from corrected reflection data.

The same procedure is repeated for each observed saturated resonant peak. Finally, $\tilde{n}$ is accurately obtained from corrected transmission in all regions of transparency, while in the absorption peaks, we set $\tilde{n} = \tilde{n}_R$. An example is given in **Figure 11** (right). An 890-μm thick pellet of pure maltose has been characterized by THz-TDS. In the vicinity of the absorption peaks at 1.15, 1.65, and 2.05 THz, transmission of the sample is below the noise level. In these spectral ranges, we save the value of $\tilde{n}_R$ extracted from corrected reflection data, while in the other

http://dx.doi.org/10.5772/66348

regions of transparency, we retain the phase-corrected transmission values $\tilde{n}_T$. Absorption peaks as high as 250 cm^{-1} can be precisely evaluated.

6. Combined transmission THz-TDS and Kramers-Kronig analysis

Reflection schemes are sometimes not available with commercial systems, preventing any phase correction procedure as detailed in the previous paragraph. Fortunately, phase jumps can be corrected from transmission measurements only. The causality of THz response of natural materials makes possible to calculate $n(\omega)$ from $\alpha(\omega)$ with the Kramers-Kronig (KK) relations. In fact, the phase jumps, due to saturation of transmission in the absorption peaks, impact mainly the extraction of $n(\omega)$ and very slightly $\alpha(\omega)$ outside the absorption bands. Thus, the idea [30] here is to extract $\alpha(\omega)$ from TDS data in the transparency spectral regions and to perform a KK calculation to get $n(\omega)$. Missing $\alpha(\omega)$ values (in the absorption peak) induce an error on $n(\omega)$, which is quite small because it is spread over the spectrum thanks to the integral KK calculation. Comparing, in the transparency regions, $n(\omega)$ determined by the KK transformation and the one extracted from THz-TDS data permits to know and correct the phase jumps occurring at each resonance, if any. A last extraction, with the phase corrected transmission TDS data, leads to a very precise determination of $n(\omega)$ between the absorption peaks. In fact, THz-TDS data are obtained over a limited spectral range, while KK calculation should be completed from 0 to infinity. The resulting error is minimized by performing a singly subtractive Kramers-Kronig (SSKK) transform [31]:

$$n(\omega) = n\left(\omega_a\right) + \frac{c}{\pi} PP \int_0^{\infty} \frac{\alpha(\omega')\left(\omega^2 - \omega_a^2\right)}{\left(\omega'^2 - \omega_a^2\right)\left(\omega'^2 - \omega_a^2\right)} d\omega' \tag{26}$$

PP stands for "principal part." The SSKK transformation requires knowing the refractive index at a given angular frequency, namely, the anchorage angular frequency ω_a. When dealing with THz spectra exhibiting saturated peaks, employing SSKK has two advantages: to minimize errors due to a limited experimental bandwidth, and to take advantages of the precisely known value $n\left(\omega_a\right)$ as long as ω_a is chosen before the first saturated peak. This technique combining transmission THz-TDS and KK analysis has been used to retrieve the refractive index of a 790-μm thick DAST sample. The refractive index n_{SSKK} has been calculated from α_T with an anchorage frequency f_a = 0.5 THz, and compared to the optical parameters extracted from a 235-μm thick DAST sample (dashed curves), which do not suffer from any saturation effects. Because of the large absorption peaks of DAST centered at 1.1 and 3.1 THz, no transmitted signal was detected around these peaks. As seen in **Figure 12**, this results in a saturation of the absorption peaks together with an offset of $n_T(\omega)$, determined by a classical THz-TDS extraction, after the low transmission bands. The SKKK method leads to a corrected spectrum $n_{SSKK}(\omega)$, which however suffers from a small discrepancy due to missing $\alpha(\omega)$ data. But $n_{SSKK}(\omega)$ is sufficiently close to the actual $n(\omega)$, which permits to find the phase jump value by comparing $n_{TDS}(\omega)$ and $n_{SSKK}(\omega)$, and then to perform again a classical extraction with the phase corrected over the saturated peak frequencies.

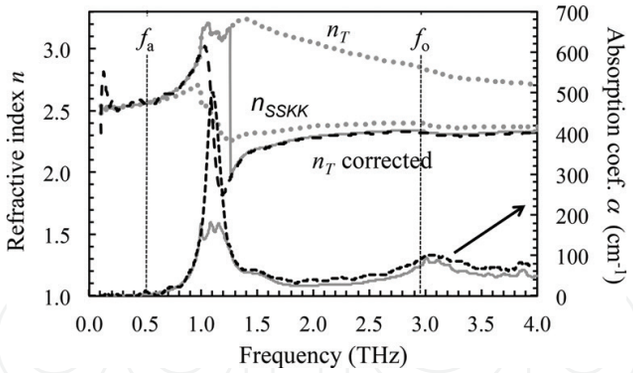

Figure 12. n_T and α_T of DAST extracted from transmission THz-TDS measurements of a 790-μm thick sample, and the refractive index corrected by the SSKKR method (solid line), by evaluating the $2m\pi$ phase jump at $f_0 = 2.95$. n_{SSKK} (attention n et pas eta) has been calculated from α_T with an anchorage frequency $f_a = 0.5$ THz. These results are compared with the ones obtained with a 235-μm thick DAST sample (dashed curves) that does not suffer from any saturation effect.

7. Scattering effect

When dealing with chemical compounds, many samples are pellets fabricated by pressing a powder mixture of the material to be studied and of a transparent hosting matrix. This technique permits to characterize materials (named hereafter "inclusion" material) that are extremely absorbent in the THz range, or that cannot be manufactured as bulky or film samples, or that could be dangerous at a high concentration. The optical parameters (refractive index and absorption coefficient) of the inclusion material, diluted in the hosting powder, are retrieved through a model describing the electromagnetism response of the mixture. If this mixture can be considered as homogeneous, i.e., if powder grains and more generally inhomogeneity are smaller than the wavelength, there is no scattering: the electromagnetic response of the material can be described by effective medium theories. Among many theories, the most popular models are the Maxwell-Garnett one (MG) [32] and the Bruggmann (BG) one [33]: the inclusions are supposed to be spheroids or ellipsoids embedded in the hosting matrix. According to these models, the dielectric constant of the mixture respectively obeys:

$$\mathrm{MG}: \varepsilon_{\mathrm{mixture}} = \varepsilon_{\mathrm{host}} \frac{2(1-p)\varepsilon_{\mathrm{host}} + (1+2p)\varepsilon_{in}}{(2+p)\varepsilon_{\mathrm{host}} + (1-p)\varepsilon_{in}}, \tag{27}$$

$$\mathrm{BG\ (spheroids)}: \quad (1-p)\frac{\varepsilon_{\mathrm{host}} - \varepsilon_{\mathrm{mixture}}}{\varepsilon_{\mathrm{host}} + 2\,\varepsilon_{\mathrm{mixture}}} + p\,\frac{\varepsilon_{in} - \varepsilon_{\mathrm{mixture}}}{\varepsilon_{in} + 2\,\varepsilon_{\mathrm{mixture}}} = 0. \tag{28}$$

p is the volume concentration of the inclusions. Basically, MG models allow one to nicely fit experimental data when both p and the contrast $\varepsilon_{\mathrm{in}}/\varepsilon_{\mathrm{host}}$ remain small. For larger contrasts, the Bruggeman's model is preferable. **Figure 13** (left) shows the real part of the permittivity, at 0.6 THz, of a mixture of HDPE and fructose powder versus the volume fraction of fructose. Both MG (continuous line) and Bruggeman (dashed line) models well fit the experimental data (open circles), because scattering effects do not affect so much the time of flight of the THz beam across the sample, i.e., the real refractive index n. On the other hand, the

imaginary part of the permittivity (**Figure 13**, right) cannot be fitted by a MG model because scattering losses, which are not taken into account in the MG theory, are misinterpreted as absorption.

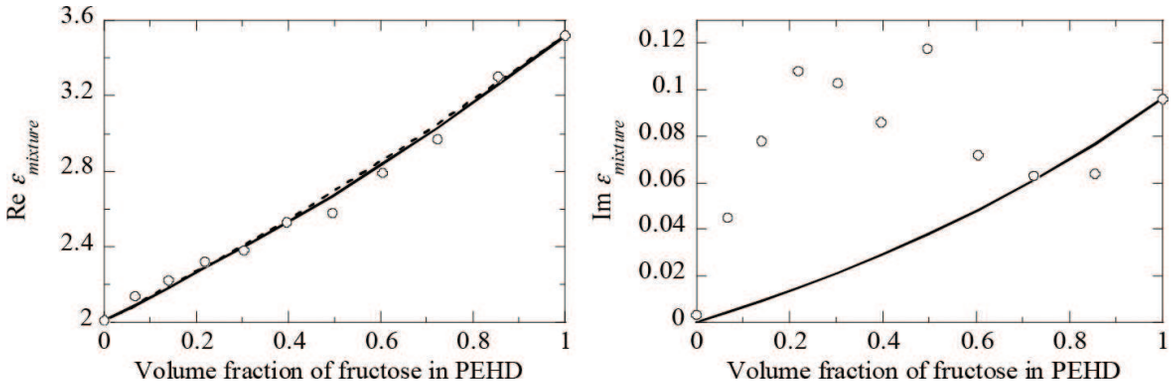

Figure 13. Real part (left) and imaginary part (right) of the permittivity $\varepsilon_{\text{mixture}}$ of a mixture of HDPE and fructose powders versus the volume fraction of fructose at 0.6 THz. Open circles: experimental data; continuous line: MG model; dashed line: BG model.

Thus, in many heterogeneous samples, scattering occurs and depends on the relative size of the scattering particles as compared to the wavelength [34]. If the particle size is smaller than about $\lambda/20$, scattering may be neglected while, if it is bigger than about $10 \times \lambda$, rays are geometrically deviated by powder grains. In between these limits, when particles are smaller than the wavelength, the scattering process is well described by the Rayleigh theory, while Mie scattering occurs for grain size comparable or bigger than the wavelength. Because of the typical size of the grains in common powders, Rayleigh scattering is almost negligible at THz frequencies and Mie scattering [35] model or even more complicated theories must be employed. As there is no analytical expression available to render the scattered amplitude, numerical codes are used. Nevertheless, Mie theory can be approximated at low scatterer concentration by simplified models, like the one proposed by Raman [36] to explain the Christiansen effect [37]. In this case, the equivalent absorption is expressed as:

$$\alpha_{\text{scattering}} = \Delta K^2 f^2 \left(n_{in} - n_{\text{host}}\right)^2. \tag{29}$$

Δ is the average size of the scattering grains and K is a coefficient that depends on the shape, the concentration, and the distribution of the grains. Such model is established on the probability, at one dimension, that an incoming photon is scattered by a grain. It shows a loss variation proportional to the square frequency. Multiple scattering is not entered into the theory, which means that the absorption coefficient of a sample does not depend on its thickness. **Figure 14** (left) illustrates the scattering effect in mixtures of HDPE and sugars (fructose, maltose, glucose). At the lowest frequencies, absorption obeys a f^2-law (dashed lines). Let us point out that the f^2-dependence is also the behavior of Mie-type scattering,

which should be considered. **Figure 14** (right) shows the absorption of a HDPE-maltose mixture corrected from scattering to be compared to absorption obtained with a pure maltose sample.

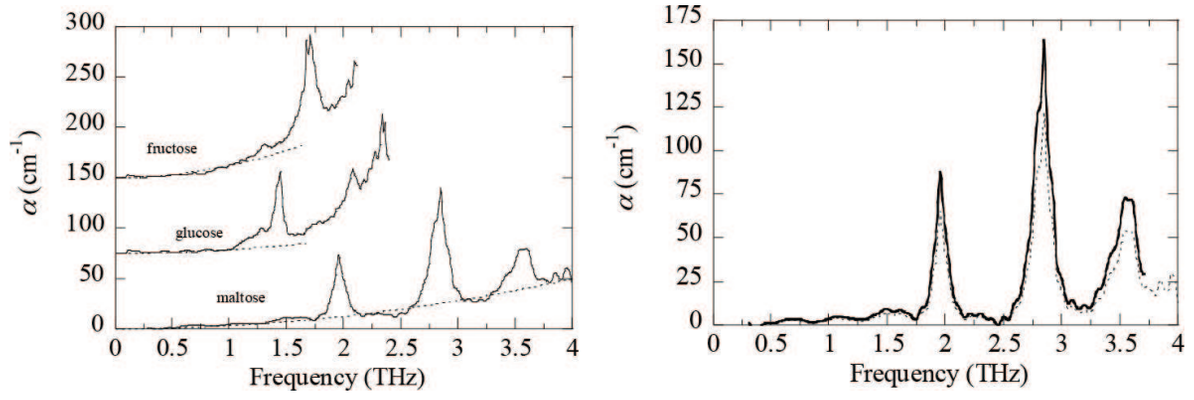

Figure 14. Left: Absorption of a mixture of powders of 25% of HDPE and 75% of sugars (maltose, glucose, and fructose) versus frequency. For the sake of visibility, the glucose and fructose curves are vertically shifted of 75 and 150 cm^{-1}, respectively. The dashed lines are parabolic fitting curves; (right) absorption of maltose (continuous) and HDPE-maltose mixture (dashed) corrected from scattering.

The limit of validity of the Raman model is also shown in **Figure 15**. The measured absorption of the mixture is plotted versus the volume fraction p of fructose (**Figure 15**, left).

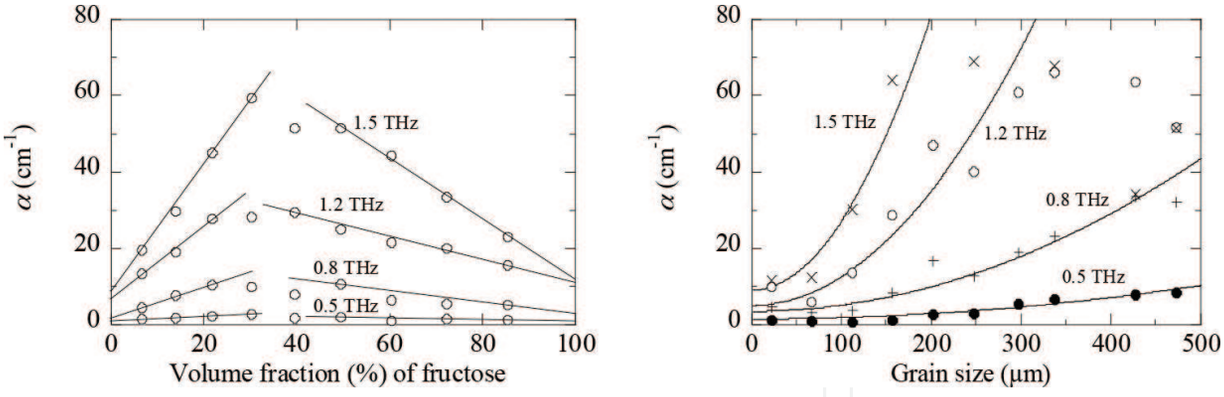

Figure 15. Left: Measured absorption of a mixture HDPE-fructose powder mixture versus the volume fraction p of fructose at different frequencies. The lines are a guide to the eye; (right) measured absorption of a mixture HDPE-fructose powder mixture (p = 30%) versus the size Δ of the fructose grain at different frequencies. The lines are parabolic fits.

At different frequencies, the experimental data are well fitted by a linear curve for p < 20–30% and for p > ~50%, (28). In between, the transition fructose-in-HDPE to HDPE-in-fructose cannot be described by the Raman model. **Figure 15** (right) presents the measured absorption

http://dx.doi.org/10.5772/66348

versus the size Δ of the fructose grains, for a constant volume ratio p = 30%. The experimental points are fitted by parabolic curves, which do not obey to relation (29), except at the limit Δ→0. A more rigorous modeling of the scattering process in such mixtures is based on the Mie scattering theory. Several numerical codes are freely available to estimate the Mie scattering, like the one from the Oregon Medical Laser Center [38]. **Figure 16** exhibits the extinction coefficient, taking into account both absorption and scattering losses, at 1.5 THz of a HDPE-fructose mixture (p = 30%). Mie modeling gives a curve (dotted line) below the experimental data (dots), when the bulk value n_{HDPE} = 1.51 is entered in the calculation. A better fit is obtained with n_{HDPE} = 1.41. Such a result could be explained by residual air inclusions (20%) in the pellet which decrease the effective refractive index of the host substance [39]. The agreement between experimental data and calculated ones is good, especially as no adjustable parameter is input in the calculation. Moreover, some geometrical factors cannot be taken into account, like for example the shape of the fructose grains, which looks like cubes instead of spheres as required to apply Mie hypothesis.

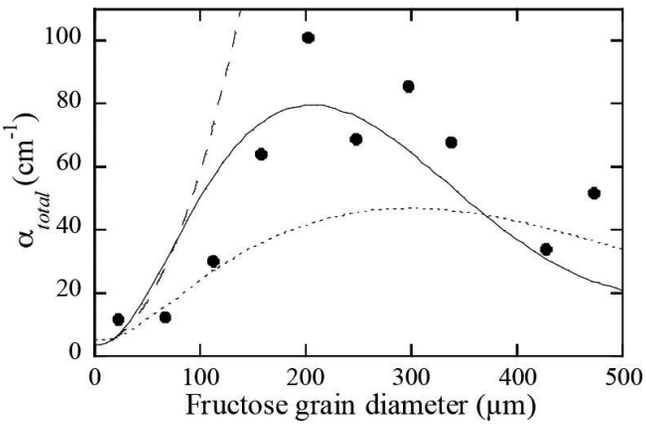

Figure 16. Absorption, including scattering, of a mixture of HDPE-fructose (p = 30%) determined from transmission THz-TDS (dots). The lines are calculated with a Mie scattering code [39]: with n_{HDPE} = 1.51 (dotted), with n_{HDPE} = 1.41 (continuous). The dashed line is a parabolic dependence at small grain sizes.

8. Conclusion

We have described here the main features of THz-TDS. This is a unique technique to quantitatively and precisely characterize the electromagnetic response of materials and devices over a broadband in the far-infrared domain. However, because of limited space, we did not address in this chapter some additional possibilities of THz-TDS in terms of material characterization:

- Anisotropic materials: Their characterization by THz-TDS is not tricky as most of THz antennas (photo-conducting switches or electro-optic crystals) are polarization-sensitive, with a rather good rejection level (a few percent). Even cross-polarization effects can be investigated by rotating the receiving antenna around the optical axis of the THz system.

Moreover, THz-TDS supplies the phase of the transmitted signals with respect to the involved THz beam polarization, from which the anisotropic parameters of a sample can be deduced.

- Metamaterials: They are quite easy to manufacture for the THz range, as they require repetitive features whose size is smaller than the wavelength, i.e., in the range below a few tens of microns. This is achieved with MEMS or/and microelectronics technologies. Such THz metamaterials [40] show amazing properties, like negative refractive index (left-handed property), chirality, and so on. THz-TDS is especially well adapted to characterize these metamaterials because it delivers both amplitude and phase of the reflected or/and transmitted signal. Thus, for example, a negative phase, due to propagation in a left-handed material, is clearly observed in the THz-TDS experimental spectra.
- Time-resolved THz-TDS [41]: This technique can be applied if the sample under test is sensitive to light. In this case, a third part of the pulsed laser beam illuminates the sample with an adjustable delay as compared to the impinging THz pulse. The light-induced modification of the sample properties, mostly by photo-generation of free carriers, changes the transmission of the THz beam. By varying the optical-THz time-delay, the photo-induced excitation in the material is time resolved. This method works very well to study the carrier dynamics in semiconductors and in superconductors, as far as the carrier lifetime is not too short as compared to the THz pulse duration. The main limitation of the technique is the rather long duration of the THz pulse, i.e., few hundreds of femtoseconds, as compared to very fast phenomena in matter. Investigating short events requires a proper deconvolution of the temporal records, which is not an easy task.

The list of applications of THz-TDS is for sure quite long and giving it exhaustively is almost impossible. Moreover, the continuous progress of technology makes the technique really easy to use, especially with commercial systems, and numerous new scientific results are regularly published.

Author details

Maxime Bernier*, Frédéric Garet and Jean-Louis Coutaz

*Address all correspondence to: maxime.bernier@univ-savoie.fr

Laboratory IMEP-LAHC, UMR CNRS 5130, University of Savoie Mont-Blanc, Savoy, France

References

[1] Bell R. J.; Introductory Fourier Transform Spectroscopy, 1972, Academic Press, New York.

[2] Auston D. H., Chueng K. P.: Coherent time-domain far-infrared spectroscopy. J. Opt. Soc. Am. B. 1985; **2**: 606–612.

[3] van Exter M., Fattinger Ch., Grischkowsky D.: Terahertz time-domain spectroscopy of water vapor. Opt. Lett. 1989; **14**: 1128–1130.

[4] Pastol Y., Arjavalingam G., Halbout J.-M., Kopcsay G. V.: Coherent broadband microwave spectroscopy using picosecond optoelectronic antennas. Appl. Phys. Lett. 1989; **54**: 307–309.

[5] Mittleman D., editor, Sensing with terahertz radiation, Springer Series in Optical Sciences, 2003 (Vol. 85).

[6] Sakai K., editor, Terahertz Optoelectronics, Springer Topics in Applied Physics, 2005 (Vol. 97).

[7] Zhang X.-C. and Xu J., Introduction to THz Wave Photonics, Berlin: Springer 2009.

[8] Lee Y.-S., Principles of Terahertz Science and Technology, Berlin: Springer 2009.

[9] Bründermann E., Hübers H.-W., and Kimmitt M., THz techniques, Springer Series in Optical Sciences, 2012 (Vol. 151).

[10] China: Oplan (www.oplanchina.com); Germany: Batop (www.batop.de), Menlo Systems (www. menlosystems.com), Accurion (www.accurion.com), Toptica (www.toptica.com), LaserQuantum/GigaOptics (www.laserquantum.com); Japan: Advantest (www.advantest.co.jp); Lithuania: Ekspla-Teravil (www.ekspla.com); Switzerland: Rainbow Photonics AG (www.rainbowphotonics.com); UK: Bruker-TeraView (www.teraview.com); USA: Zomega (www.zomega-terahertz.com), Del Mar Photonics (www.delmarphotonics.com), Picometrix (www.picometrix.com), Emcore (www.emcore.com), ARP (http://arphotonics.net), MicroTech Instruments Inc. (www.mtinstruments.com).

[11] Ho I.-C., Guo X., Zhang X.-C. : Design and performance of reflective terahertz air-biased-coherent-detection for time-domain spectroscopy. Opt. Expr. 2010; **18**: 2872–2883.

[12] Vieweg N., Fischer B. M., Reuter M., Kula P., Dabrowski R., Celik M. A., Frenking G., Koch M., Jepsen P. U.: Ultrabroadband terahertz spectroscopy of a liquid crystal. Opt. Expr. 2012; **20**: 28249–28256.

[13] Matsubara E., Nagai M., Ashida M.: Coherent infrared spectroscopy system from terahertz to near infrared using air plasma produced by 10-fs pulses. J. Opt. Soc. Am. B. 2013; **30**: 1627–1630.

[14] Nemec H., Kadlec F., Kuzel P.: Methodology of an optical pump-terahertz probe experiment: An analytical frequency-domain approach. J. Chem. Phys. 2002; **117**: 8454–8466.

[15] Ulbricht R., Hendry E., Shan J., Heinz T. F., Bonn M.: Carrier dynamics in semiconductors studied with time-resolved terahertz spectroscopy. Rev. Mod. Phys. 2011; **83**, 543–586.

[16] Beard M. C., Schmuttenmaer C. A.: Using the finite-difference time-domain pulse propagation method to simulate time-resolved THz experiments. J. Chem. Phys. 2001; **114**: 2903–2909.

[17] Beard M. C., Turner G. M., Schmuttenmaer C. A.: Terahertz spectroscopy. J. Phys. Chem. 2002; **106**: 7146–7159.

[18] Leitenstorfer A., Nelson K. A., Reimann K., Tanaka, K.: Focus on nonlinear terahertz studies. New Journal of Physics. 2014; **16**, 045016.

[19] Krotkus A., Coutaz J.-L.: Non-stoichiometric semiconductor materials for terahertz optoelectronics applications. Semicond. Science Techn. 2005; **20**: S142.

[20] Hirori, H., Yamashita K., Nagai, M., Tanaka K.: Attenuated total reflection spectroscopy in time domain using terahertz coherent pulses. Japanese journal of applied physics. 2004; **43**: L1287.

[21] Duvillaret L., Garet F., Coutaz J.-L.: A reliable method for extraction of material parameters in terahertz time-domain spectroscopy. IEEE J. Sel. Top. Quant. Electron. 1996; **2**: 739–746.

[22] Withayachumnankul W., Fischer B. M., Lin H., Abbott D.: Uncertainty in terahertz time-domain spectroscopy measurement. J. Opt. Soc. Am. B. 2008; **25**: 1059–1072.

[23] Pashkin A., Kempa M., Nemec H., Kadlec F., Kuzel P.: Phase-sensitive time-domain terahertz reflection spectroscopy. Rev. Sci. Instrum. 2003; **74**: 4711–4717.

[24] Khazan M., Meissner R., Wilke I.: Convertible transmission-reflection time-domain terahertz spectrometer. Rev. Sci. Instrum. 2001; **72**: 3427–3430.

[25] Nagashima T., Hangyo M.: Measurement of complex optical constants of a highly doped Si wafer using terahertz ellipsometry. Appl. Phys. Lett. 2001; **79**: 3917–3919.

[26] Thrane L., Jacobsen R. H., Jepsen P. U., Keiding S. R.: THz reflection spectroscopy of liquid water. Chem. Phys. Lett. 1995; **240**: 330–333.

[27] Lucarini V., Ino Y., Peiponen K.-E., Kuwata-Gonokami M.: Detection and correction of the misplacement error in terahertz spectroscopy by application of singly subtractive Kramers-Kronig relations. Phys. Rev. B. 2005; **72**: 125107.

[28] Hoshina H., Seta T., Iwamoto T., Hosako I., Otani C., Kasai Y.: Precise measurement of pressure broadening parameters for water vapor with a terahertz time-domain spectrometer. J. of Quant. Spectr. Rad. Transfer. 2008 ; **109**: 2303–2314.

[29] Bernier M., Garet F., Coutaz J.-L.: Precise Determination of the Refractive Index of Samples Showing Low Transmission Bands by THz Time-Domain Spectroscopy. IEEE Trans. THz Sci. Technol. 2013 ; **3**: 295–301.

[30] Bernier M., Garet F., Coutaz J.-L.: Accurate characterization of resonant samples in the terahertz regime through a technique combining time-domain spectroscopy and Kramers-Kronig analysis. IEEE Trans. THz Sci. Technol. 2016 ; **6**: 442–450.

[31] Lucarini, V., Saarinen, J. J., Peiponen, K. E., & Vartiainen, E. M.: Kramers-Kronig relations in optical materials research. Springer Science & Business Media 2005 (Vol. 110).

[32] Garnett J. C. M. : Colours in metal glasses and in metallic films. Phil. Trans. R. Soc. Lond. 1904; **203**: 385.

[33] A. G. Bruggeman: Berechnung verschiedener physikalischer Konstanten von heterogenen Substanzen. Ann. Phys. (Leipzig). 1935; **24**: 636–679.

[34] Menzel, W. P. Remote sensing applications with meteorological satellites. Online lecture of University of Wisconsin-Madison, Space Science and Engineering Center, Cooperative Institute for Meteorological Satellite Studies; 2005.

[35] Mie G.: Annalen der Physik. 1908; **330**: 377.

[36] Raman C. V., Viswanathan K. S. Proc. Indian Acad. Sci. A.1955; **41**: 55.

[37] Franz M., Fischer B.M., Walther M.: The Christiansen effect in terahertz time-domain spectra of coarse-grained powders. Appl. Phys. Lett. 2008; **92**: 021107–01.

[38] Available from: http://omlc.ogi.edu/software/mie/

[39] Garet F., Hofman M., Meilhan J., Simoens F., Coutaz J.L.: Evidence of Mie scattering at terahertz frequencies in powder materials. App. Phys. Lett. 2014; **105**: 031106.

[40] Yen T. J., Padilla W. J., Fang N., Vier D. C., Smith D. R., Pendry J. B., Basov D. N., Zhang X.: Terahertz magnetic response from artificial materials. Science. 2004; **303**,1494–1496.

[41] Groeneveld R. H. M., Grischkowsky D.: Picosecond time-resolved far-infrared experiments on carriers and excitons in GaAs-AlGaAs multiple quantum wells. J. Opt. Soc. Am. B. 1994; **11**: 2502–2507.

IntechOpen